

# Supervised classification of etoposide-treated *in vitro* adherent cells based on noninvasive imaging morphology

Anna Leida Mölder,<sup>a,\*</sup> Johan Persson,<sup>b</sup> Zahra El-Schich,<sup>b</sup> Silvester Czanner,<sup>a</sup> and Anette Gjørloff-Wingren<sup>b</sup>

<sup>a</sup>Manchester Metropolitan University, School of Computing, Mathematics and Digital Technology, Faculty of Science and Engineering, Manchester, United Kingdom

<sup>b</sup>Malmö University, Department of Biomedical Science, Health and Society, Malmö, Sweden

1  
2  
3

**Abstract.** Single-cell studies using noninvasive imaging is a challenging, yet appealing way to study cellular characteristics over extended periods of time, for instance to follow cell interactions and the behavior of different cell types within the same sample. In some cases, e.g., transplantation culturing, real-time cellular monitoring, stem cell studies, *in vivo* studies, and embryo growth studies, it is also crucial to keep the sample intact and invasive imaging using fluorophores or dyes is not an option. Computerized methods are needed to improve throughput of image-based analysis and for use with noninvasive microscopy such methods are poorly developed. By combining a set of well-documented image analysis and classification tools with noninvasive microscopy, we demonstrate the ability for long-term image-based analysis of morphological changes in single cells as induced by a toxin, and show how these changes can be used to indicate changes in biological function. In this study, adherent cell cultures of DU-145 treated with low-concentration (LC) etoposide were imaged during 3 days. Single cells were identified by image segmentation and subsequently classified on image features, extracted for each cell. In parallel with image analysis, an MTS assay was performed to allow comparison between metabolic activity and morphological changes after long-term low-level drug response. Results show a decrease in proliferation rate for LC etoposide, accompanied by changes in cell morphology, primarily leading to an increase in cell area and textural changes. It is shown that changes detected by image analysis are already visible on day 1 for 0.25- $\mu$ M etoposide, whereas effects on MTS and viability are detected only on day 3 for 5- $\mu$ M etoposide concentration, leading to the conclusion that the morphological changes observed occur before and at lower concentrations than a reduction in cell metabolic activity or viability. Three classifiers are compared and we report a best case sensitivity of 88% and specificity of 94% for classification of cells as treated/untreated. © 2017 Society of Photo-Optical Instrumentation Engineers (SPIE) [DOI: 10.1117/1.JMI.4.2.XXXXXX]

Keywords: single-cell studies; noninvasive microscopy; low-concentration etoposide; digital image cytometry; digital holographic microscopy; cell classification.

Paper 16160SSR received Jul. 31, 2016; accepted for publication Feb. 20, 2017.

## 1 Introduction

When treating an organism with a substance *in vivo*, cells will typically be exposed to a variety of concentrations, depending on their location within the tissue and the body. Cells will also react differently when exposed to the same concentration depending on their cell type, tissue type, and sometimes stage in the cell cycle. Most assays in use today study the average characteristics of large groups of cells and are unable to show the variability of the cell population. Single cells can be studied using time-lapse imaging, with or without fluorescent markers or dyes or using nonimaging marker-based techniques, such as flow cytometry. The use of markers in cell imaging has several disadvantages. It is indirect and invasive, and also makes the cells unusable for further tests. In some cases, this is not preferable, such as in studies of tissue or cells for transplantation, the study of embryonic cells and stem cells, or when the sample needs to be kept in a continuously viable condition for a longer study. The study of single cells *in vivo* during long periods of time requires the development of nondisturbing measurement

techniques in combination with appropriate methods of analysis, many of which have yet to be developed. We evaluate one such technique, where standard image analysis and classification are combined with noninvasive microscopy and applied to a toxicology study using etoposide, a cytotoxic drug with well-described physiological effects. Etoposide is a chemotherapeutic drug commonly used as an anticancer agent, causing DNA damage and eventually triggering cell death by apoptosis at high concentrations. The process at subapoptotic concentrations and during long-term exposure is yet poorly understood, but reports of effects include drug resistance and risk of secondary leukemia (Sec. 1.1). To study the effects of long-term low-level exposure, it is necessary to use an imaging set-up, where the same cells can be monitored over time.

This study was motivated by the desire to be able to detect the treatment concentration of etoposide by means of nondestructive image analysis of adherent cells *in situ* for long periods of time on a cell-by-cell basis by means of morphological cues (Fig. 1) induced by the toxin. We use a combination of digital holographic microscopy (DHM) and image analysis to profile

\*Address all correspondence to: Anna Leida Mölder, E-mail: [mail@annaleida.com](mailto:mail@annaleida.com)

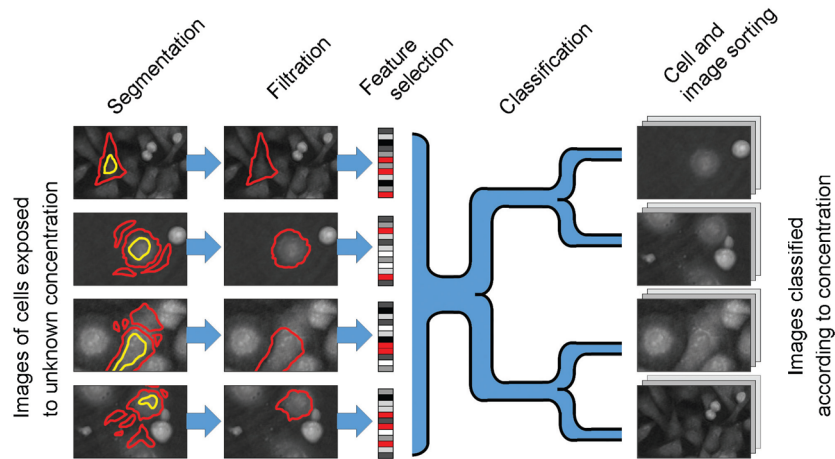


**Fig. 1** Algorithmic overview of the classification of cells exposed to a treatment, based on their imaged morphological characteristics. Images are segmented and filtered, features extracted and used to train a supervised classifier.

morphological changes in DU-145 cells,<sup>1,2</sup> which we induce by exposure to low-concentration (LC) etoposide, and model the cells as a set of image-derived feature parameters. Cross correlation with the known result is used to determine the most prominent set of features. We then use the model to classify the cells to the ground-truth treatment concentrations, and in the end, we compare the result to that of a standard bulk assay, the MTS, for reference. The classification is made on a cell-by-cell basis with cells from cultures exposed to different concentrations of etoposide. Cells are also combined using the average over all cells in images from one sample in order to make it possible to compare the results with the MTS assay, where the evaluation is made on a culture-by-culture basis. The MTS assay is a colorimetric method for sensitive quantification of viable cells in proliferation and cytotoxicity assay. It is based on reduction of the MTS solution, a tetrazolium compound, by viable cells to generate a colored formazan product that is soluble in cell culture media and detectable using a spectrophotometer. The conversion is presumably accomplished by NADPH or NADH produced by dehydrogenase enzymes in metabolically active cells.<sup>3</sup>

### 1.1 Etoposide Toxic Effects

Etoposide has a long history as an anticancer agent<sup>4</sup> and is usually administered intravenously or orally in capsule form. Etoposide has been reported to cause cell cycle arrest, which has been tested previously using DHM.<sup>5,6</sup> It functions by interaction with the enzyme topoisomerase II, causing breaks in the DNA strand, ultimately leading to apoptosis,<sup>7,8</sup> a process in which cells also undergo morphological changes.<sup>9,10</sup> Etoposide is one of the most widely used chemotherapeutic agents for several types of cancer,<sup>11–13</sup> but its effect is limited by toxicity.<sup>11</sup> It is shown<sup>14</sup> that both the  $\alpha$  and  $\beta$  types of topoisomerase II are targeted by etoposide, but only at concentrations above or equal to  $1 \mu\text{M}$ , although some growth inhibition was observed at lower concentrations. Bleibel et al.<sup>15</sup> reported half maximal inhibitory concentrations (IC<sub>50</sub>) slightly below  $1 \mu\text{M}$ , suggesting that effects are also present at LC of etoposide. These conclusions are confirmed by Liu et al.,<sup>16</sup> who also found that a lower limit for etoposide-induced proliferation and viability reduction occurs at  $\sim 0.02 \mu\text{M}$  and also shows effects on the

cell cycle at concentrations  $< 1 \mu\text{M}$  (although for different cell lines). Even lower concentrations were reported to cause changes in phenotype and potentially also cause drug resistance or cause secondary leukemia.<sup>17</sup>

### 1.2 Digital Holography

Dennis Gabor was the first to invent a way to encode the phase of the light in a single recording, i.e., the hologram.<sup>18</sup> The technique was later used as base for the development of digital holography.<sup>19–22</sup> Some years later, the first DHM images showing living cells were published.<sup>23</sup> Digital holography is a full-field imaging technique, where pixel values are directly related to cellular dry mass, and as the images from a mathematical point of view are similar to those from a standard epifluorescence microscope, the same image analyzing algorithms can often be used. In cellular biology, DHM has been used for a number of applications, including *in vivo* studies,<sup>24</sup> subcellular motion within living tissue,<sup>25</sup> migration studies,<sup>26–29</sup> studies of morphological changes,<sup>30–33</sup> proliferation,<sup>34</sup> and apoptosis.<sup>35</sup> Figure 2 shows an example of typical morphological changes in DU-145 cells treated with etoposide and compared with the control.

## 2 Materials and Methods

### 2.1 Cell Culture

DU-145 cells (ATCC<sup>®</sup> HTB-81, ATCC LGC Standards, Teddington, United Kingdom) were grown in 75 cm<sup>2</sup> flasks in Dulbecco's modified Eagle's medium (DMEM, Invitrogen, Carlsbad, California) cell culture media with an added 10% fetal calf serum. Cells were subcultivated twice per week to keep the culture nonconfluent.

### 2.2 Digital Holographic Microscopy Image Capture

For DHM tests,  $2 \times 10^4$  cells per well were seeded in 6-well plates (day 1). After 24-h incubation to allow the cells to attach, fresh media with the desired concentration etoposide (Sigma-Aldrich Co., St. Louis, Missouri dissolved in dimethyl sulfoxide (DMSO) (Sigma-Aldrich) was added (day 0). Images of cells were captured at days 1 to 3. The experiment was repeated for

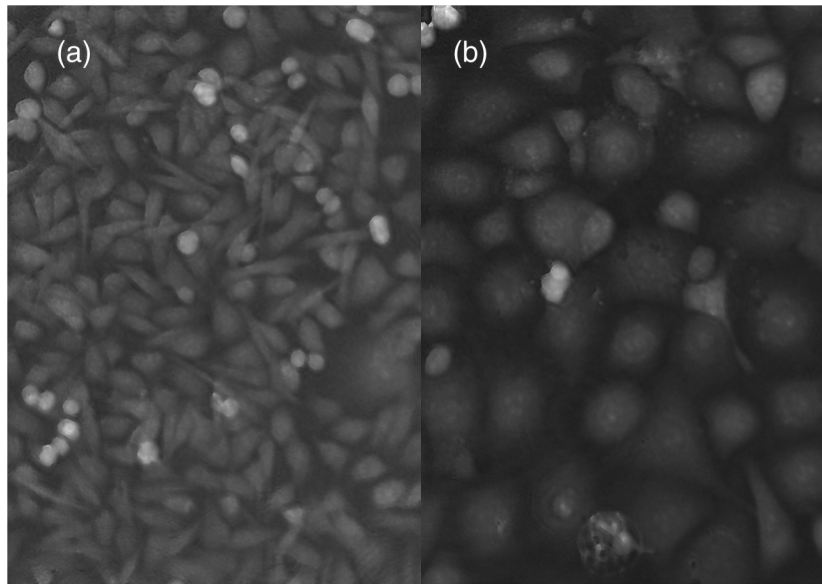


**Fig. 2** Example of DU-145, (a) control and (b) 72 h after treatment with 0.5- $\mu$ M etoposide, imaged with digital holography. Image intensity is related to an optical phase shift, which is in turn related to cellular dry mass.

etoposide concentrations  $c = 0.25, 0.5, 1, \text{ and } 5 \mu\text{M}$ . As DMSO was used to dissolve etoposide, two controls were used: untreated cells and cells in only DMSO. DHM images were captured using HoloMonitor M4 (Phase Holographic Imaging AB, Lund, Sweden), using a 635-nm, 0.2 mW/cm<sup>2</sup> laser as the light source. The 6-well plate was taken out of the incubator, the lid was removed, and 15 images were captured from each well, after which the lid was replaced and the plate was returned to the incubator. All DHM images are 1024  $\times$  1024 pixels, at a scale of 0.51  $\mu\text{m}$ /pixel.

### 2.3 MTS Assay

Cells were seeded (day 1) into a 96-well plate at a density of  $5 \times 10^3$  cells per well in 100  $\mu\text{l}$  of cell culture medium. Six wells per test condition were used. All unused wells were filled with media including a blank column. After incubating for 24 h to allow the cells to attach, the media was substituted for new media with the desired test concentration (day 0). After 24, 48, and 72 h, the plate was then analyzed using the MTS assay. Etoposide was tested at  $c = 0.25, 0.5, 1, \text{ and } 5 \mu\text{M}$ , respectively. As the etoposide was dissolved in DMSO, a column with only DMSO equal to the amount in the wells with the most DMSO (i.e., the wells with the highest concentration of etoposide) was used as a secondary control. Twenty microliters of MTS (Promega Corporation, Madison) was added to each well and mixed by tapping the side of the plate. After incubating for 1 h and then again after 2 h, the plate was read using BIO-TEK microplate reader at 490 nm.

### 2.4 Image Analysis

To identify single cells as regions of interest (ROI), images were segmented with the microscope software HoloStudio™ (Phase Holographic Imaging AB, Lund, Sweden), using a seeded watershed segmentation.<sup>36</sup> The half-elliptical shape of attached adherent cells results in a thicker central part of each cell. Using DHM, this is seen as a stronger signal, and it is straightforward

to extract cell centers using a combination of Gaussian smoothing and H-maxima transform. The detected centers can then be used as seeds. The original image, after applying a minimum threshold (further described below) and inverting, is used as image input for the watershed. The purpose of the threshold is to reduce noise and somewhat flatten the image background (the bottom of the cell culture vessel) and define cell borders. After the watershed is complete and in a final noise reduction step, segmented objects smaller than 20 pixels were discarded. The most crucial step of the segmentation is the threshold setting prior to segmentation. In this study, two implementations were used. Otsu thresholding (OT)<sup>37</sup> yielded a higher cut-off than minimum error thresholding (MET),<sup>38</sup> resulting in a more accurate pinpointing of cells as out-of-focus debris in the growth medium was not selected. On the other hand, MET gave a more accurate cell outline (Fig. 3). In order to maintain the accuracy of the border segmentation given in MET, while at the same time restrict the selection to actual cells (and not sample contamination or image artifacts), we introduced a new preprocessing step, where we use both segmentation methods in combination. The location of cells given by the segmentation using OT was used to filter the noncellular bodies from the segmentation using MET, thus gaining the advantages of both methods.

We then proceeded to extract a set of gray-level image features from each ROI to use as input for classification. The purpose of this was to reduce the information in the image (given as pixel by pixel) to only relevant variables for cell  $n$ ,

$$v(n) = (v_1, v_2, \dots, v_m, \dots, v_{M-1}, v_M), \quad (1)$$

where  $M$  is the number of variables gathered. We first collected a set of 22 standard grayscale variables and cross correlated them with the known result, using sample means. The features for the treated cells that showed average differences from control with a confidence of 95%,  $P < 0.05$ , were chosen for the model and then used to classify single cells. A mathematical definition of the selected variables is given in Sec. 2.6.

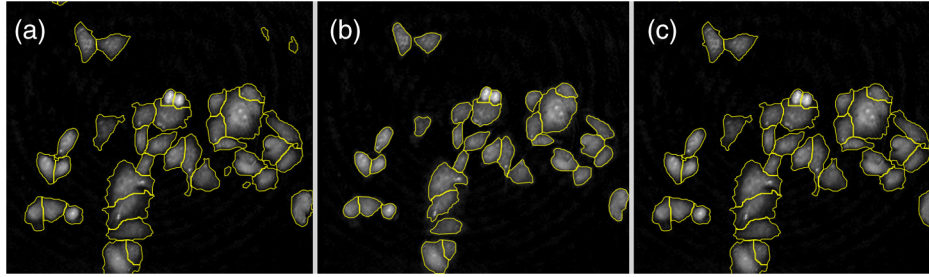


**Fig. 3** Cell filtering using double thresholding. The same image (control day 1) segmented using (a) MET, (b) OT, and (c) the result of MET, filtered using the OT to identify cells.

## 2.5 Proliferation

An estimate of the number of cells per culture vessel was calculated each day from the cell count given by the image analysis. The number of cells was determined as the number of segmented bodies in an image, using the MET after filtering by OT, as described in Sec. 2.4. It has previously been shown that a count using image analysis of DHM images is comparable to operator cell counting using a Bürker chamber<sup>34</sup> and using the image-based method instead of the manual, it is possible for us to perform all measurements over 3 days in the same culture vessel, not only saving time during the analysis but also removing one potential source of error.

## 2.6 Image Features

Define the original image  $F(x, y)$ , with dimensions  $X$  and  $Y$ , respectively, as a two-dimensional matrix of gray levels  $i$ , to a maximum gray level  $I$ . Let  $\psi$  be the subset of  $F$  belonging to the ROI of one cell selected in the segmentation (i.e., the area), with perimeter  $\rho$ . Define each element of the gray-level co-occurrence matrix (GLCM)  $P(i, j)$  of  $F$  as the number of times gray level  $F(x, y) = i$  is oriented with respect to gray level  $F(x+1, y+1) = j$ , where  $i, j \in [0, G]$ , and  $G < I$  is the number of gray levels used in the GLCM. In our case,  $G = 8$ . The result is an intermediate matrix, whose values indicate how often one pixel value in  $F(x, y)$  tends to be similar to its adjacent values. We normalize the GLCM so that

$$\sum_{i=1}^G \sum_{j=1}^G [P(i, j)] = 1. \quad (2)$$

In this way, each value in  $P(i, j)$  will denote the probability of a range of gray levels to appear in each others' proximity. We assume the cells to be randomly oriented, so we satisfy ourselves with computing only one GLCM along the horizontal ( $x$ ) direction. For calculation of a roughness distribution  $R(x, y)$ , for each  $\psi$  we compute

$$R = F(x, y) - \Omega[F(x, y)], \quad (3)$$

where  $\Omega$  is a Gaussian smoothing filter, and  $(x, y) \in \psi$ . Features calculated from the GLCM are mean, standard deviation, energy (angular second moment), entropy, contrast, and correlation.<sup>39</sup> In addition, the following features are used for classification:

Cell area:

$$A = \sum_x \sum_y 1, (x, y) \in \psi, \quad (4)$$

Perimeter length:

$$P = \sum_x \sum_y 1, (x, y) \in \rho, \quad (5)$$

Phase shift integral:

$$\Phi_{\text{tot}} = \sum_x \sum_y F(x, y), \quad (6)$$

Roughness kurtosis:

$$R_k = \frac{1}{A} \frac{\sum_x \sum_y [R(x, y) - \bar{R}]^4}{\sigma^4}, \quad (7)$$

Roughness skewness:

$$R_s = \frac{1}{A} \frac{\sum_x \sum_y [R(x, y) - \bar{R}]^3}{\sigma^3}, \quad (8)$$

Texture homogeneity:

$$S_{\text{hom}} = \sum_{i=1}^G \sum_{j=1}^G \frac{P(i, j)}{1 - |(i - j)|^2}, \quad (9)$$

where  $\sigma$  is used to denote standard deviation and  $\bar{R}$  is the average over the roughness  $R$ .

## 2.7 Classification

In order to classify single cells, we used three different methods and attempted to classify cells into one of five classes, one for each concentration of etoposide used. Methods used were a multiclass support vector machine (SVM), a Naïve Bayes classifier, and a classification tree using random forests (RFs). For the SVM, a linear kernel was used, and the hyperplane determined by sequential minimal optimization.<sup>40</sup> A multiclass SVM was then constructed by combining binary SVMs pairwise in a directional acyclic graph.<sup>41</sup> The Naïve Bayes classifier used a normal Gaussian distribution estimating the prior probabilities from the relative frequencies of the training classes.<sup>42</sup> The RF used the classification and regression tree algorithm,<sup>43</sup> and the optimization criterion was minimization of node impurity as defined by Gini's diversity index. In order to reduce tree complexity and avoid overfitting, we request that the tree (for 5-bin classification) should have maximum 20 and minimum nine nodes. Nine is the minimum number of nodes (including leaves) a binary classification can contain with classification into five bins. Very rarely, the tree from the training contained  $\geq 30$  nodes,

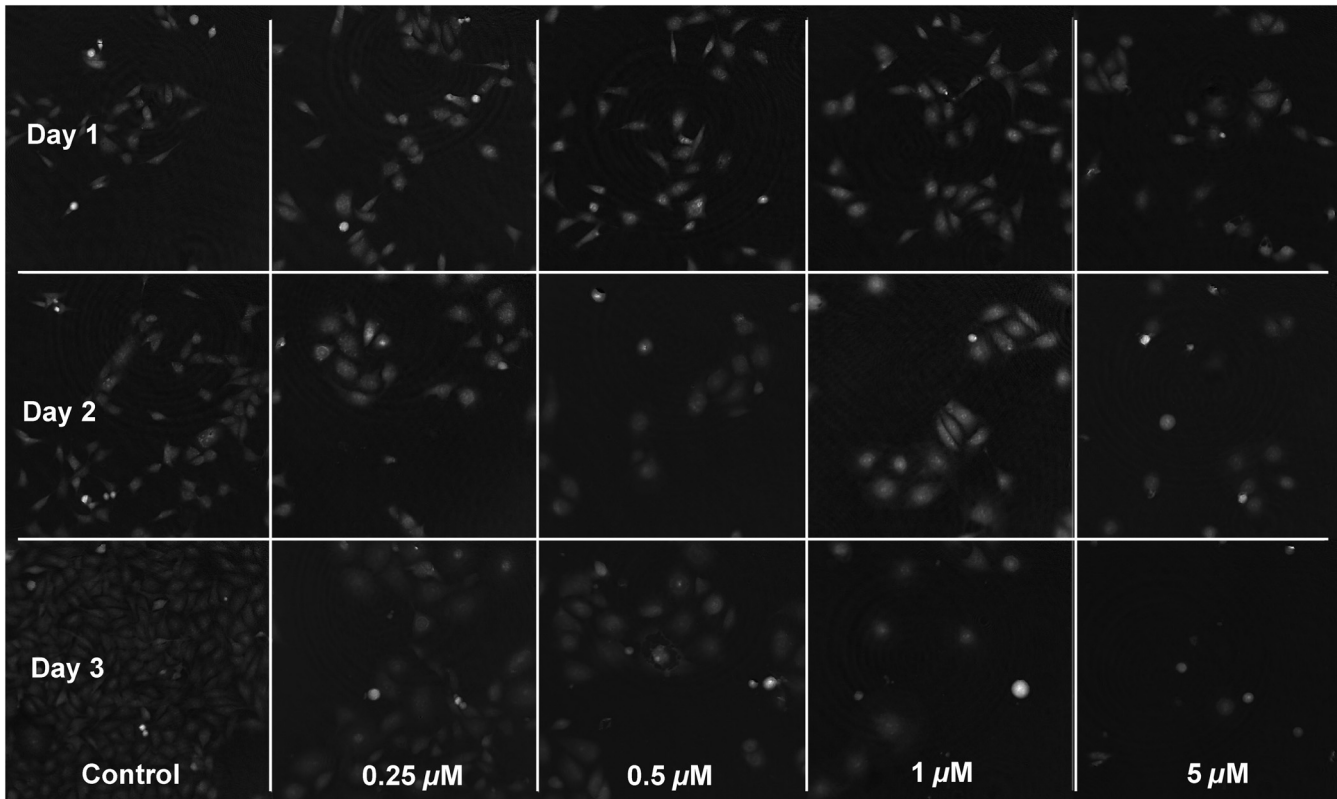


**Fig. 4** Typical appearance of DU-145 imaged by digital holography after several days exposure to LC-etoposide treatment.

severely overfitting the training data. A tree of 20 nodes will classify into 13 bins and was chosen arbitrarily to be a large enough number to cover any reasonable classification of 5 except obvious misses. Typical numbers of nodes were 10 to 15 per tree. For all methods, the training cells [rows of  $v(n)$ ] were selected randomly as 10% of the total number of available  $N$  cells for that sample. The rest of the cells (the validation set) were used to test the accuracy of the result by cross correlation. The process of training and testing was repeated ten times, and the results were averaged. The performance was evaluated using a standard 4 core PC with 8-GB RAM, with the code implemented in MATLAB R 7.12.0.635 (R2011a).

## 2.8 Statistics

Errors are given as 95% confidence intervals, unless otherwise stated. To compute the  $P$  values, a two-tailed t-test was performed. Experiments were repeated three times for concentration  $0.25 \mu\text{M}$ , four times for  $0.5 \mu\text{M}$ , twice for  $1 \mu\text{M}$ , and once for  $5 \mu\text{M}$ . In 90 samples, a total of 66495 cells were imaged, averaging 738 cells per sample.

## 3 Results

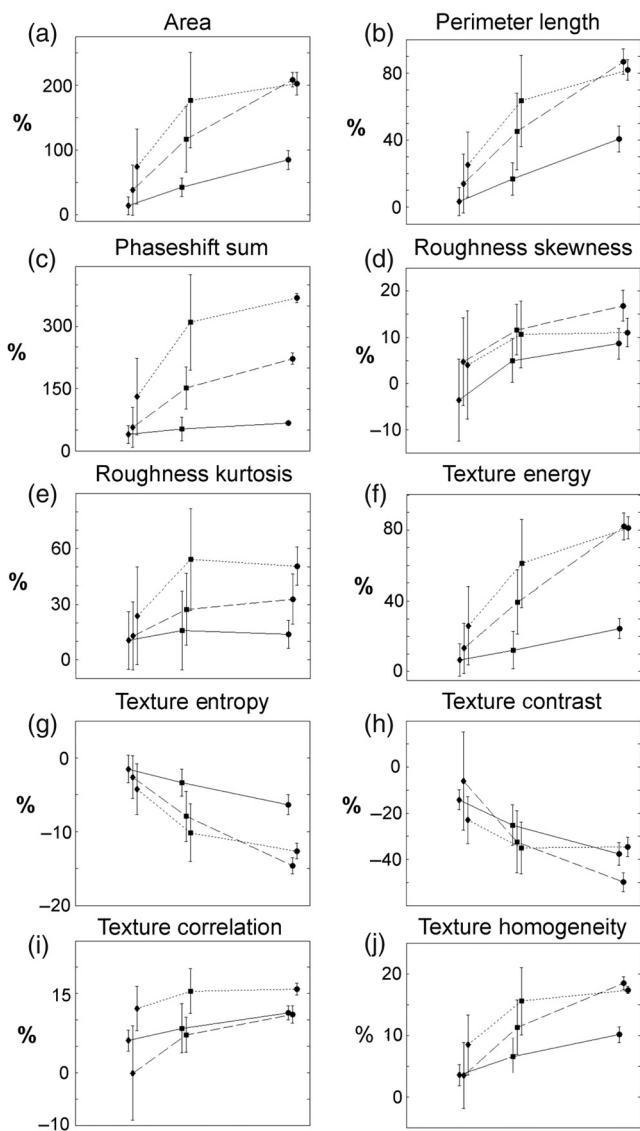
### 3.1 Observed Morphological Changes

Figure 4 shows typical changes in cell morphology for all five concentrations of etoposide (including control) from day 1 to day 3 after treatment. The control cells show normal exponential cell growth, filling the culture vessel by day 3. Healthy cells display a compact spindle or prolonged elliptic shape throughout, with uniform cell size from day 1 to day 3. The  $5\text{-}\mu\text{M}$

concentration shows the most distinct case of toxicity, with immediate arrest in cell growth and reduction in cell number at days 2 and 3. Cell shapes are slightly round in day 1 and mostly spherical in days 2 and 3 and are detached from the bottom of the cell culture vessel. Concentrations from  $0.25$  to  $1 \mu\text{M}$  show intermediate stages of varying severity. Images from  $1 \mu\text{M}$  day 2,  $0.25 \mu\text{M}$  day 3, and  $0.5 \mu\text{M}$  days 2 and 3 show similar morphological changes. These changes, which appear to be consistent with onset of or low-level exposure to etoposide toxicity have a rounded, flattened shape and increased cell area with cells still attached to the bottom of the cell culture vessel. In some cases, an increased granularity can be seen within cells, though this may be caused by the increased area and flatness, giving a higher contrast to variations in internal cellular structure than can be seen in the healthy compact elliptical shape. Qualitatively, it appears as if cell proliferation has been halted at this stage, but with little or no increase in cell mortality, and the cell number is approximately constant. In order to quantitatively study differences of etoposide-treated cells, we averaged the features over all cells in each sample (Fig. 5) and compared them to control. Most prominent were the differences for area, perimeter length, and the integral of the phase shift. Physically, these components are all related to the cell size, which is consistent with the qualitatively observed changes.

### 3.2 MTS Correlation and Proliferation

From the daily segmentation of images, we obtain a count of cell proliferation (Fig. 6). The cell growth for the control was close to exponential, and a reduction in cell growth rate was detectable for etoposide concentrations of  $5 \mu\text{M}$ , consistent with the MTS



**Fig. 5** Variable values compared with control, calculated from sample-wise mean. Day 1 (solid), day 2 (dashed), and day 3 (dotted) after treatment. x-axis represents etoposide concentration; 0.25  $\mu\text{M}$  (diamond), 0.5  $\mu\text{M}$  (square), and 1  $\mu\text{M}$  (circle), respectively. Error bars represent standard deviation, and for clarity, each series has been slightly offset in x-direction. a) Area, b) Perimeter length, c) Phaseshift sum, d) Roughness skewness, e) Roughness kurtosis, f) Texture energy, g) Texture entropy, h) Texture contrast, i) Texture correlation, j) Texture homogeneity.

results (Fig. 7). It is notable that the morphological changes were already detectable on day 1 with DHM for all examined concentrations of etoposide, whereas changes in MTS absorbance are only detectable for the highest concentration of etoposide (5  $\mu\text{M}$ ) on day 3.

### 3.3 Cell Classification

With the five separate concentrations of etoposide, we had five bins available for classification, but in a real-life situation, we do not expect to know the concentration of the sample. In these cases, it is of more interest to ask whether a sample is exposed to some concentration  $c$  higher than some minimum value,  $c \geq c_{\min}$ . In this case, the task is reduced to the binary problem

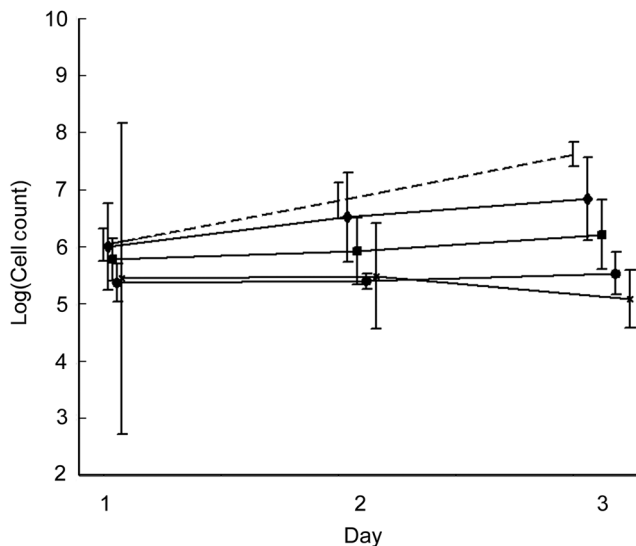


**Fig. 6** Proliferation curves for DU-145 under the effect of etoposide 0  $\mu\text{M}$  (dashed), 0.25  $\mu\text{M}$  (diamond), 0.5  $\mu\text{M}$  (square), 1  $\mu\text{M}$  (circle), and 5  $\mu\text{M}$  (cross). Measurements were taken at the same time, and values for x-axis have been displaced slightly to display confidence intervals.

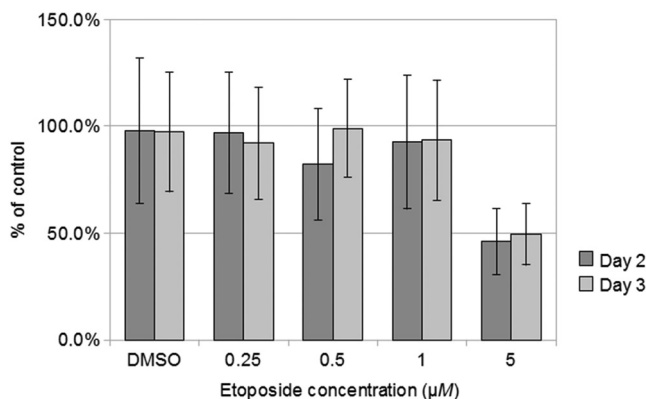


**Fig. 7** MTS absorbance as % of control days 2 and 3, as a function of etoposide concentration, after 2 h of MTS incubation.

of classifying cells as being treated ( $c \geq c_{\min}$ ) or not treated ( $c < c_{\min}$ ). We use the sensitivity and specificity as indicators of classification quality

$$\text{Sensitivity} = \frac{E(c \geq c_{\min}) \cup T(c \geq c_{\min})}{T(c \geq c_{\min})}, \quad (10)$$

$$\text{Specificity} = \frac{E(c < c_{\min}) \cup T(c < c_{\min})}{T(c < c_{\min})}, \quad (11)$$

here,  $E(c)$  is the set of cells being classified as concentration  $c$ , and  $T(c)$  is the set of cells actually exposed to concentration  $c$ . There was a tendency for concentrations to be underestimated and also a lower probability of separating control and 0.25  $\mu\text{M}$ , as well as of separating higher concentrations from each other. We show a best case classification in separating control from treated (etoposide  $< 0.25 \mu\text{M}$ ) at sensitivity and specificity of

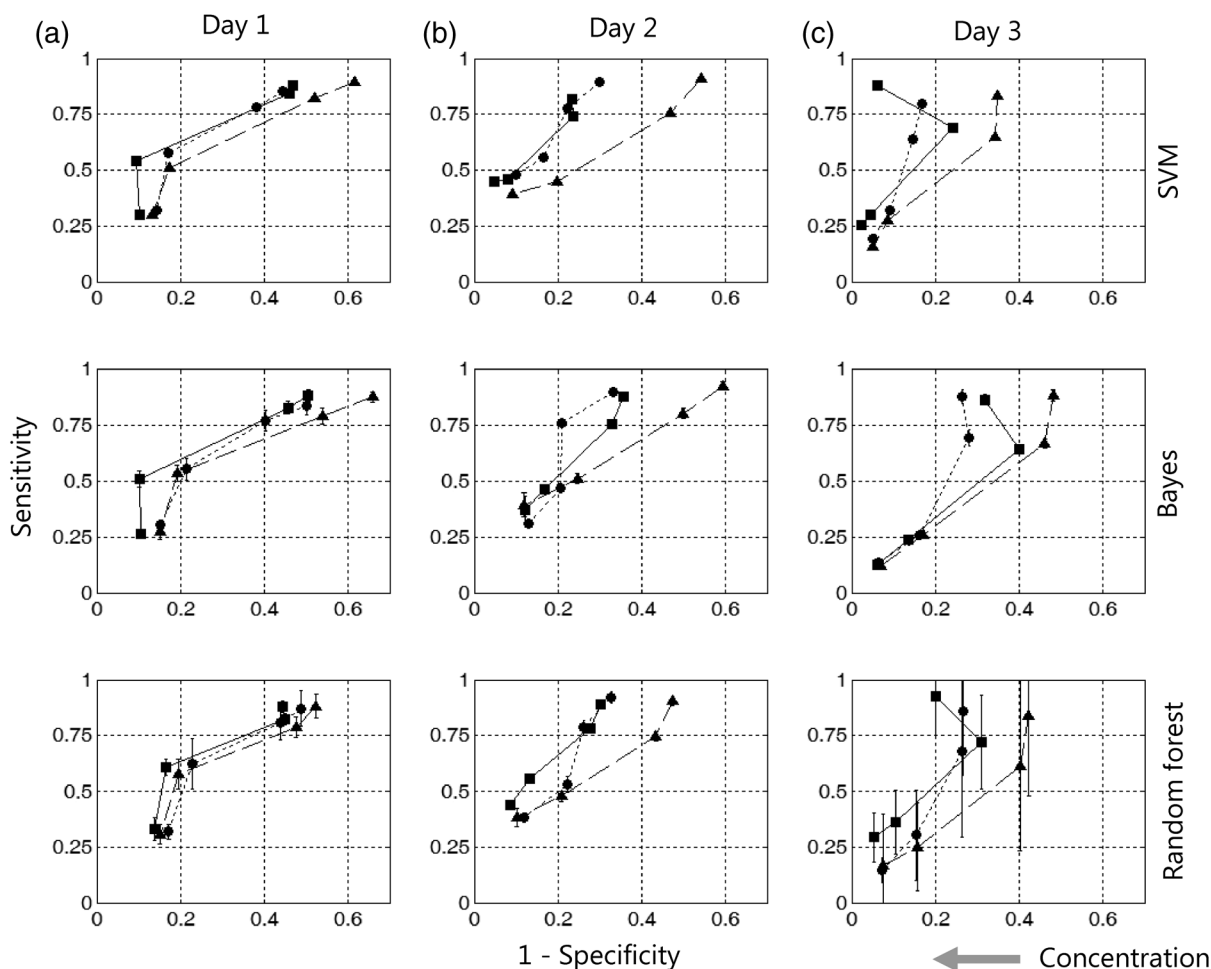


**Fig. 8** ROC for classification of cells exposed to etoposide (concentration increasing from right to left as indicated in figure). Classifications used are SVM (top row), Naïve Bayes (middle row), and RF (bottom row). Segmentation thresholds used are Otsu (solid square), minimum error (dashed triangle), and filtered (dotted circle). Results have been grouped according to the day of measurement taken (a)–(c).

88% ± 0.17 and 94% ± 0.001, respectively, for multiclass SVM using OT. The skewness in accuracy describes a case with more false negatives than false positives. The results are similar for days 1 and 2, with incrementally reduced sensitivity and simultaneously increased specificity at higher concentrations. Figure 8 shows the receiver operating characteristics (ROC) for classification based on the two original segmentation methods, compared with the version with spatial filtering of cells for all 3 days and methods of classification. The data on 5 μM were very scarce due to very low number of cells in each image (typically <10 cells), giving wide confidence intervals in the results. The specificity was improved throughout days 1 to 3 for all classifiers, reflecting the fact that cell morphology becomes more and more distinct (Fig. 4). In most cases, the multiclass SVM was the best classifier. It was closely matched by an RF, but the errors for the RF were higher, especially when cell morphology differed strongly. For day 1, there was only a marginal difference between the three segmentation methods, but for days 2 and 3, the filtered thresholding gave the most reliable classification for LC, and the OT is the most reliable classification for higher concentrations (≥1 μM). We note a significant improvement in specificity between 0.25 and 0.5 μM, most visible in day 3 for Otsu and filtered thresholdings, but visible for all classifiers

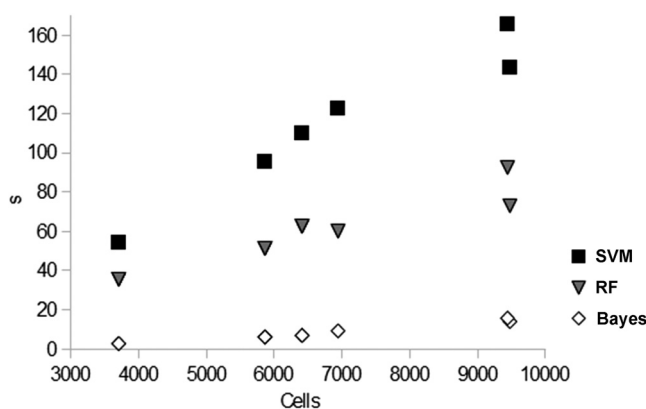


**Fig. 9** Performance (computation time in seconds) for three classifiers; SVM, Naïve Bayes, and RF as function of number of cells classified.

and thresholds, reflecting the fact that cell morphology changes more rapidly at these concentrations. The computational performance of the Naïve Bayes classifier was an order of magnitude better than that of the SVM (Fig. 9), whereas the RF ranked between these two methods.

## 4 Discussion

We have demonstrated a method for image analysis, single-cell segmentation, and cell classification for the analysis of drug response of adherent *in vitro* cells over long periods of time. We show that the changes induced are possible to detect at an individual cell level and that analysis of morphological features of cell systems under certain circumstances can be used to test for changes in biological function. The morphological changes observed do not directly correlate with the chemical assay, but rather show complementary information. The key elements of the method are a nondestructive optical set-up and a robust image analysis, segmentation, and classification. We chose a seeded watershed segmentation because of its simplicity and availability, but other segmentation methods may have worked equally well. However, a common trait for all is the correct location of cell border, which had a large impact on classification performance. In our case, this was influenced by the fact that one of the most prominent effects of LC-etoposide exposure was the increase in cell area. For higher concentrations of etoposide, the OT gave the most reliable classification, whereas for lower concentrations (in the region, where only the morphological changes were detected), the filtered thresholding, with cell borders defined by the MET, gave a comparable or better result. This can be due to the fact that cell area is larger for treated cells and that the classification is improved by a thresholding, which includes the cell perimeter.

Given the low overall probability to pinpoint the exposure concentration of a single cell (for LC etoposide, a sensitivity in the range of 70% to 90% with some exceptions), the SVM seems to be the best choice of classifier, despite its longer computational time. The classification of concentrations  $\geq 0.25 \mu\text{M}$  and control was the most reliable. For future experiments, we would like to further examine the range of lower concentrations ( $< 0.25 \mu\text{M}$ ). In our investigation, we focused on lower concentrations of etoposide, where cell growth is inhibited, but cell number is not severely reduced, and this is reflected in the low cell number available for analysis of the higher concentrations etoposide ( $\geq 1 \mu\text{M}$ ). The sensitivity of higher concentrations etoposide could be readily increased by obtaining more images per cell culture vessel, at the cost of longer capture time.

Except for the feature selection for the cell model, which was done by directly cross correlating with the known result, the parameters for both segmentation and classification were deliberately selected to be as little restrictive as possible by what is known of the nature of the sample. This fact contributed to the low sensitivity of the classification rate, and it may be possible to achieve much higher accuracy by specifically tailoring the analysis to expected phenotypical changes. The most obvious way to achieve more detailed cell study would be an increase in the microscope resolution. This would make it possible to more accurately study cell interior, but would reduce the number of cells available per image.

The most significant biological finding of this study is the characterization of morphological changes at LC in the 0.25- to  $1\text{-}\mu\text{M}$  range of etoposide, where no effects are detectable by MTS absorbance. The cell area is the most dominating morphological effect of long-term LC-etoposide exposure, but textural changes are also prominent. The reasons for these changes have yet to be examined, but may be connected to cell cycle arrest, as they are accompanied by a reduction in proliferation rate. Here, it is shown that changes are not directly related to reduction in viability or metabolism, as detected by MTS.

For the three lowest concentrations, no reduction in viability was detected for the 3 days examined. For all concentrations, a reduction in proliferation rate accompanied that of morphological changes. For a future investigation, it would be of interest to let the incubation proceed to investigate if viability changes would occur in time. Also, by interrupting the exposure to etoposide, it would be possible to examine if the effects of etoposide are reversible or not.

The most important technical contribution is the demonstration of the usefulness of noninvasive image analysis when examining long-term processes. For the purpose of obtaining data over a long term, the system shows excellent promise. We are able to study cells in the same sample over a 3-day period, making it possible to study any changes occurring before they are detectable by chemical assays. Performing all measurements in the same culture vessel also removes the potential source of error of using parallel samples. For the purpose of classifying single cells depending on toxin exposure, the system is less well suited, mainly due to the variety in individual morphology of cells being larger than that induced by the toxin. This stresses the fact that for individual cell studies, each cell must be tracked throughout the sequence in order to detect changes in appearance. One application for such a method is the study of single cells continuously within the same culture. This possibility opens up a whole new perspective on cellular research, where cells are viewed not as a uniform mass, but rather as a broad spectrum of individual bodies, all contributing in its own way to the characteristics of the tissue.

### Disclosures

No conflicts of interest, financial or otherwise, are declared by the authors.

### Acknowledgments

The authors would like to thank Gabriela Czanner for invaluable comments on the statistics. Economically, this work was made possible by funding from the Faculty of Science and Engineering, Manchester Metropolitan University, Manchester, UK, and Malmö University, Malmö, Sweden.

### References

1. K. R. Stone et al., "Isolation of a human prostate carcinoma cell line (DU-145)," *Int. J. Cancer* **21**, 274–281 (1978).
2. M. M. Webber, D. Bello, and S. Quader, "Immortalized and tumorigenic adult human prostatic epithelial cell lines: characteristics and applications part I," *Prostate* **29**, 386–394 (1996).
3. M. V. Berridge and A. S. Tan, "Characterization of the cellular reduction of 3-(4, 5-dimethylthiazol-2-yl)-2, 5-diphenyltetrazolium bromide (MTT): subcellular localization, substrate dependence, and involvement of mitochondrial electron transport in MTT reduction," *Arch. Biochem. Biophys.* **303**, 474–482 (1993).
4. K. R. Hande, "Etoposide: four decades of development of a topoisomerase II inhibitor," *Eur. J. Cancer* **34**, 1514–1521 (1998).
5. Z. El-Schich et al., "Digital holographic microscopy innovative and non-destructive analysis of living cells," in *Microscopy, Science, Technology, Applications and Education*, A. Méndez-Vilas and J. Díaz, Eds., pp. 1055–1062, Formatex Research Center, Badajoz, Spain (2010).
6. M. Falck Minitis, A. Mukwaya, and A. Gjörlöf Wingren, "Digital holographic microscopy for non-invasive monitoring of cell cycle arrest in L929 cells," *PLoS One* **9**, e106546 (2014).
7. L. A. Zwelling, "DNA topoisomerase II as a target of antineoplastic drug therapy," *Cancer Metastasis Rev.* **4**, 263–276 (1985).

8. S. W. Lowe et al., "p53-dependent apoptosis modulates the cytotoxicity of anticancer agents," *Cell* **74**, 957–967 (1993).
9. G. Kroemer et al., "Classification of cell death: recommendations of the nomenclature committee on cell death," *Cell Death Differ.* **12**, 1463–1467 (2005).
10. D. V. Krysko et al., "Apoptosis and necrosis: detection, discrimination and phagocytosis," *Methods* **44**, 205–221 (2008).
11. E. L. Baldwin and N. Osheroff, "Etoposide, topoisomerase II and cancer," *Curr. Med. Chem.: Anti-Cancer Agents* **5**, 363–372 (2005).
12. H.-G. Kopp et al., "Advances in the treatment of testicular cancer," *Drugs* **66**, 641–659 (2006).
13. J. R. Rigas and P. N. Lara, "Current perspectives on treatment strategies for locally advanced, unresectable stage III non-small cell lung cancer," *Lung Cancer* **50**, S17–S24 (2005).
14. E. Willmore et al., "Etoposide targets topoisomerase IIalpha and IIbeta in leukemic cells: isoform-specific cleavable complexes visualized and quantified *in situ* by a novel immunofluorescence technique," *Mol. Pharmacol.* **54**, 78–85 (1998).
15. W. K. Bleibel et al., "Identification of genomic regions contributing to etoposide-induced cytotoxicity," *Hum. Genet.* **125**, 173–180 (2009).
16. W. M. Liu, P. R. Oakley, and S. P. Joel, "Exposure to low concentrations of etoposide reduces the apoptotic capability of leukaemic cell lines," *Leukemia* **16**, 1705–1712 (2002).
17. K. C. Stine et al., "Secondary acute myelogenous leukemia following safe exposure to etoposide," *J. Clin. Oncol.* **15**, 1583–1586 (1997).
18. D. Gabor, "A new microscopic principle," *Nature* **161**, 777–778 (1948).
19. U. Schnars and W. Jptner, "Direct recording of holograms by a CCD target and numerical reconstruction," *Appl. Opt.* **33**, 179 (1994).
20. E. Cuche, P. Marquet, and C. Depeursinge, "Simultaneous amplitude-contrast and quantitative phase-contrast microscopy by numerical reconstruction of Fresnel off-axis holograms," *Appl. Opt.* **38**, 6994–7001 (1999).
21. J. W. Goodman, "Digital image formation from electronically detected holograms," *Appl. Phys. Lett.* **11**, 77–79 (1967).
22. M. Kronrod, N. Merzlyakov, and L. Yaroslavskii, "Reconstruction of a hologram with a computer," *Sov. Phys.-Tech. Phys.* **17**, 333–334 (1972).
23. P. Yu et al., "Holographic optical coherence imaging of tumor spheroids," *Appl. Phys. Lett.* **83**, 575–577 (2003).
24. H. Sun et al., "Visualization of fast-moving cells *in vivo* using digital holographic video microscopy," *J. Biomed. Opt.* **13**, 014007 (2008).
25. K. Jeong, J. J. Turek, and D. D. Nolte, "Fourier-domain digital holographic optical coherence imaging of living tissue," *Appl. Opt.* **46**, 4999 (2007).
26. C. J. Mann, L. Yu, and M. K. Kim, "Movies of cellular and sub-cellular motion by digital holographic microscopy," *Biomed. Eng. Online* **5**, 21 (2006).
27. F. Dubois et al., "Digital holographic microscopy for the three-dimensional dynamic analysis of *in vitro* cancer cell migration," *J. Biomed. Opt.* **11**, 054032 (2006).
28. J. Persson et al., "Cell motility studies using digital holographic microscopy," in *Microscopy, Science, Technology, Applications and Education*, A. Méndez-Vilas and J. Díaz, Eds., pp. 1063–1072, Formatex Research Center, Badajoz, Spain (2010).
29. P. Langehanenberg et al., "Automated three-dimensional tracking of living cells by digital holographic microscopy," *J. Biomed. Opt.* **14**, 014018 (2009).
30. I. Moon and B. Javidi, "3-D visualization and identification of biological microorganisms using partially temporal incoherent light in-line computational holographic imaging," *IEEE Trans. Med. Imaging* **27**, 1782–1790 (2008).
31. M. Kemmler et al., "Noninvasive time-dependent cytometry monitoring by digital holography," *J. Biomed. Opt.* **12**, 064002 (2007).
32. Y. Emery et al., "DHM (digital holography microscope) for imaging cells," *J. Phys. Conf. Ser.* **61**, 1317–1321 (2007).
33. B. Kemper and G. von Bally, "Digital holographic microscopy for live cell applications and technical inspection," *Appl. Opt.* **47**, A52 (2008).
34. A. Mölder et al., "Non-invasive, label-free cell counting and quantitative analysis of adherent cells using digital holography," *J. Microsc.* **232**, 240–247 (2008).
35. Z. El-Schich et al., "Induction of morphological changes in death-induced cancer cells monitored by holographic microscopy," *J. Struct. Biol.* **189**, 207–212 (2015).
36. S. Hernandez and K. Barner, "Joint region merging criteria for watershed-based image segmentation," in *Proc. Int. Conf. on Image Processing*, Vol. **2**, pp. 108–111 (2000).
37. N. Otsu, "A threshold selection method from gray-level histograms," *IEEE Trans. Syst. Man Cybern.* **9**, 62–66 (1979).
38. J. Kittler and J. Illingworth, "Minimum error thresholding," *Pattern Recognit.* **19**, 41–47 (1986).
39. R. M. Haralick, K. Shanmugam, and I. Dinstein, "Textural features for image classification," *IEEE Trans. Syst. Man Cybern.* **SMC-3**, 610–621 (1973).
40. N. Cristianini and J. Shawe-Taylor, *An Introduction to Support Vector Machines: And Other Kernel-based Learning Methods*, Cambridge University Press, New York (2000).
41. J. C. Platt, J. Shawe-Taylor, and N. Cristianini, "Large margin DAGs for multiclass classification," in *Proc. Advances in Neural Information Processing Systems*, Vol. **12**, pp. 547–553 (1999).
42. T. Mitchell, *Machine Learning*, McGraw Hill, New York, USA (1997).
43. L. Breiman et al., *Classification and Regression Trees*, CRC Press, Boca Raton (1984).

**Anna Leida Mölder** received her MSc degree in technical engineering, her BSc degree in biology from Lund University, and received her PhD from Manchester Metropolitan University in 2016, specializing in computer analysis in medical imaging. She uses computer vision and machine learning for life science applications, with a special interest in microscopy. She is currently engaged as a senior research software engineer at the University of Manchester.

**Johan Persson** received his master of science in molecular biology from Lund University in 2008. He is a guest researcher at Malmö University. He also works in the private medical device and drug industry as a research associate in microbiology.

**Zahra El-Schich** has been a researcher in biomedical science at Malmö University since 2011. She has been performing research in different projects in immunology, cell biology, cancer, and imaging. She is also teaching immunology and supervises thesis work.

**Silvester Czanner** is principal lecturer in computing at Manchester Metropolitan University. He is doing research in areas of computer graphics, medical imaging, and digital technologies, especially their applications in education, such as using graphics, images, and animations to enable and enhance learning. He obtained his PhD in mathematics from Comenius University, in Slovakia. He is a senior member of the association for computing machinery and the director of eurographics, UK chapter.

**Anette Gjörlöf-Wingren** received her PhD in tumor immunology at Lund University in 1995. She has been an associate professor in immunology since 2002. She is performing research and education at Malmö University in immunology, morphology, cell biology, cancer, and imaging, as well as supervision and examination of thesis work at basic and advanced levels.